

Three-Dimensional Dose Prediction for Lung IMRT Patients with Deep Neural Networks: Robust Learning from Heterogeneous Beam Configurations

A.M. Barragán-Montero^{1, 2}, D. Nguyen¹, W. Lu¹, M. Lin¹, X. Geets^{2, 3}, E. Sterpin^{2, 4}, S. Jiang^{1,†}

¹Medical Artificial Intelligence and Automation (MAIA) Laboratory, Department of Radiation Oncology, University of Southwestern Texas, Dallas, TX, USA

²Center of Molecular Imaging, Radiotherapy and Oncology (MIRO), Université catholique de Louvain, Brussels, Belgium

³Department of Radiation Oncology, Cliniques universitaires Saint-Luc, Brussels, Belgium.

⁴Laboratory of Experimental Radiotherapy, Department of Oncology, KU Leuven, Leuven, Belgium.

†Correspondence author. E-mail: Steve.Jiang@UTSouthwestern.Edu

ABSTRACT

Purpose: The use of neural networks to directly predict three-dimensional dose distributions for automatic planning is becoming popular. However, the existing methods only use patient anatomy as input and assume consistent beam configuration for all patients in the training database. The purpose of this work is to develop a more general model that, in addition to patient anatomy, also considers variable beam configurations, to achieve a more comprehensive automatic planning with a potentially easier clinical implementation, without the need of training specific models for different beam settings.

Methods: The proposed *anatomy and beam* (AB) model is based on our newly developed hierarchically densely connected U-Net (HD U-Net) deep learning architecture, which combines U-Net and DenseNet. The AB model contains 10 input channels, one for beam setup and the other 9 for anatomical information (PTV and organs). The beam setup information is represented by a 3D matrix of the non-modulated beam's eye view ray-tracing dose distribution. A set of 129 lung cancer patients treated with IMRT, with very heterogeneous beam configuration (4 to 9 beams of various orientations), was used for training/validation (100 patients) and testing (29 patients). Mean squared error was used as loss function. The accuracy of the model was evaluated by comparing the mean dose, maximum dose, and other relevant dose-volume metrics for the predicted versus the clinically delivered dose distributions. Dice similarity coefficients were computed to address the spatial correspondence of the isodose surfaces between the predicted and clinically delivered doses. The model was also compared with our previous work, the *anatomy only* (AO) model, where the network does not consider beam setup information and only 9 channels for anatomical information are used.

Results: The AB model outperforms the AO model, especially in the low and medium dose regions. In terms of dose volume metrics, the improvement of AB over AO is about 1-2%. The largest improvement was found to be about 5% in lung volume receiving a dose of 5 Gy or more (V_5). The improvement for spinal cord maximum dose was also significant, i.e., 3.6% for cross-validation and 2.6% for testing. The AB model improves the Dice scores for isodose surfaces by as much as 10% in low and medium dose regions and about 2% in high dose regions.

Conclusions: The AO model, which does not use beam configuration as input, can still predict dose distributions with a reasonable accuracy in high dose regions but with large errors in low and medium dose regions, for IMRT cases with variable beam numbers and orientations. The proposed AB model achieves a significant improvement in low and medium dose regions and

a slight improvement in high dose regions over the AO model, by considering beam setup information through a cumulative non-modulated beam's eye view ray-tracing dose distribution. This new model represents a major step forward towards the prediction of 3D dose distributions in real clinical practice, where the beam configuration could vary from patient to patient, from planner to planner, and from institution to institution.

1. INTRODUCTION

Current treatment planning systems for radiation therapy use advanced software to solve an inverse optimization problem¹, which aims to determine the optimal treatment and machine parameters from an a priori specified set of dose objectives for the target and organs at risk (OARs). The fastest software can provide a solution to this problem within seconds. However, the fine tuning of the dose objectives is still done manually by the medical physicist or dosimetrist, until the desired dose distribution is achieved. This results in a heuristic and time-consuming process (from several hours to days), which entails a plan quality variability²⁻⁴ that depends on factors such as the available time to generate the plan, the institution guidelines, or the planner skills, among others. On one hand, this variability may lead to suboptimal plans that can compromise the final treatment outcome⁵⁻⁷. On the other hand, the extended treatment planning time greatly hinders the implementation of adaptive strategies^{8,9} and may delay the treatment delivery, both having a negative impact on the tumor control and patient quality of life¹⁰⁻¹³.

In order to overcome these problems, the research community has concentrated their efforts in reducing this manual component by automating the treatment planning process. Several groups have come up with powerful solutions that can be classified in two branches. The first branch relies on optimization algorithms that adjust pre-set objectives to achieve the established clinical goals, here referred to as *objective-based planning (OBP)*, with well-known implementations like the in-house software Erasmus-iCycle¹⁴ or the Auto-Planning Engine¹⁵ commercialized by Pinnacle (Philips Radiation Oncology, Fitchburg, WI), among others¹⁶⁻¹⁹. The second approach uses a library of plans from previous patients to predict dose volume objectives for the new patient²⁰⁻²³, often called *knowledge-based planning (KBP)*, with the popular commercial solution of RapidPlan (Varian Medical Systems, Palo Alto, CA). All these alternatives for automatic planning have been tested in different patient populations and sites, demonstrating a considerable speed-up of the planning process (time reduction of 70-90%), for both intensity modulated radiation therapy (IMRT) and volumetric arc therapy (VMAT)²⁴⁻²⁶, and generating high-quality plans with reduced human intervention²⁷⁻³¹.

Even with these advancements, the OBP and KBP methods still suffer from two main drawbacks. First, they use dose volume objectives, either zero-dimensional (dose volume points) or one-dimensional (dose volume histogram, DVH), for the delineated structures, which are insensitive to spatial variations of the dose within the structures and blind to those structures that are not delineated. This could lead to suboptimal plans in terms of the spatial distribution of the dose, and may require post-processing steps where the user needs to manually add planning-aid structures and re-optimize to control these spatial features. Second, both OBP and KBP strategies still require significant human intervention to define certain parameters needed to create the model, such as the target and OARs optimization goals for OBP^{14, 29, 32} or handcrafted features that serve to match the actual patient to those in the library of patients for KBP^{20, 32, 33}. Including spatial dose information³⁴⁻⁴² and completely removing manually extracted features is necessary in order to achieve a more individualized and comprehensive automatic planning.

The recent evolution of deep learning methods has motivated the use of convolutional neural networks (CNN) to predict patient specific voxel-wise dose distributions from anatomical information (i.e., contours and/or CT), either in a slice-by-slice manner (2D)^{39–41} or directly as a 3D matrix^{38, 42}. The predicted dose distribution can later be used as objective to automatically generate a treatment plan^{37, 43}. These methods completely remove the dependence on handcrafted features by allowing the deep network to learn its own features for prediction^{38–42}, and the results reported so far are very promising. However, the performance of these deep learning methods for voxel-wise dose prediction strongly depends on the database used for training, requiring to carefully choose the patients in order to have consistent beam configurations, such as VMAT³⁸ or IMRT with fixed and equally spaced beams^{39–41}. This ensures an accurate dose prediction for cases with similar beam settings, but impedes the generalization of the model to more heterogeneous beam configurations, which is crucial for IMRT treatments where the beam number and orientations could greatly vary from patient to patient and from institution to institution. In this case, the clinical implementation of automatic planning based on this type of models appears unfeasible, since it would require to generate specific models for every different beam arrangement.

As mentioned before, the current models^{38–42} use only anatomical information as input to the CNN. In this work, we investigate the added value of including both anatomical and beam setup information into the network, in order to build a single model that is robust to variable beam configuration. This general model enables to realize the full potential of deep neural networks for dose prediction, bringing closer the clinical implementation of automatic planning based on this type of methods.

2. MATERIALS AND METHODS

2. A. Model architecture

The model used for dose prediction has been developed in-house and its architecture is based on the popular U-Net, published by Ronneberger et al. in 2015⁴⁴. The U-Net is a type of CNN that belongs to the class of fully convolutional networks⁴⁵, and it is able to include both local and global features from the input images to generate a pixel-wise (two-dimensional, 2D) prediction. Our group has previously used this architecture to generate 2D dose predictions for prostate patients in a slice-by-slice manner³⁹. However, in order to avoid errors in the superior and inferior borders of the planning target volume (PTV) and OARs inherent to this 2D strategy, a three-dimensional (3D) variant of the classical 2D U-Net was developed. Since the computational load increases with the dimensionality, different models have been created in our group aiming to achieve an accurate and efficient 3D dose prediction. These models are described in detail elsewhere³⁸, and have been tested for head and neck patients. The best performance was achieved by a model that combined two recently proposed architectures: DenseNet by Huang et al. in 2017⁴⁶ and V-Net by Milletari et al. in 2016⁴⁷. The DenseNet densely connects its convolutional layers in a feed-forward fashion, using the feature-maps of all preceding layers as inputs for the current layer. This reduces the vanishing-gradient problem, enhances feature propagation and reuse, and decreases the number of trainable parameters. The drawback of this approach is the significant increase of the memory usage, entailed by the dense connection between layers. In order to maintain a reasonable RAM usage and following the work of Milletari et al., the DenseNet was modified to skip some connections between groups of layers. In addition, Huang et al.⁴⁶ found that DenseNet architectures were capable of utilizing considerably less trainable parameters than non-

densely connected architectures, yielding further RAM improvements and better generalization of the model that outweighs the increased RAM consumption of the dense connections themselves. In particular, the convolutional layers in our model are densely connected within levels of the same resolution in the U-Net, between each max pooling and up-sampling operation. We refer to each of these levels to as “hierarchy”, which motivated naming this network as Hierarchically Densely Connected U-Net (HD U-Net³⁸). This HD U-Net combines the efficient feature propagation and reuse of DenseNet, with the ability of U-Net to infer the global and local image information, while keeping a reasonable memory usage. The detailed architecture of the HD U-Net used in this study is presented in **Figure 1**, and the technical elements regarding the operations between layers has been previously described elsewhere³⁸.

The proposed model in this work, called *anatomy and beam* (AB) model, considers both patient anatomy and beam setup information as inputs. Hence, it contains 10 input channels (**Figure 1**), one channel for beam setup information and 9 channels for anatomical information. The beam setup information is represented by an approximate 3D cumulative dose distribution (ray-tracing style, beam’s eye view, and non-modulated) from all involved beams (see Section 2.D), while the anatomical information comprises 3D binary matrices or masks, i.e. the prescription dose (60 Gy) for voxels inside and 0 for voxels outside PTV, and 1 for voxels inside and 0 outside each of the 8 relevant OARs for lung treatment planning: body, heart, esophagus, spinal cord, right and left lungs, both lungs minus the target, and carina. For some patients, certain organs are not delineated, and therefore, the corresponding channel receives an empty entry.

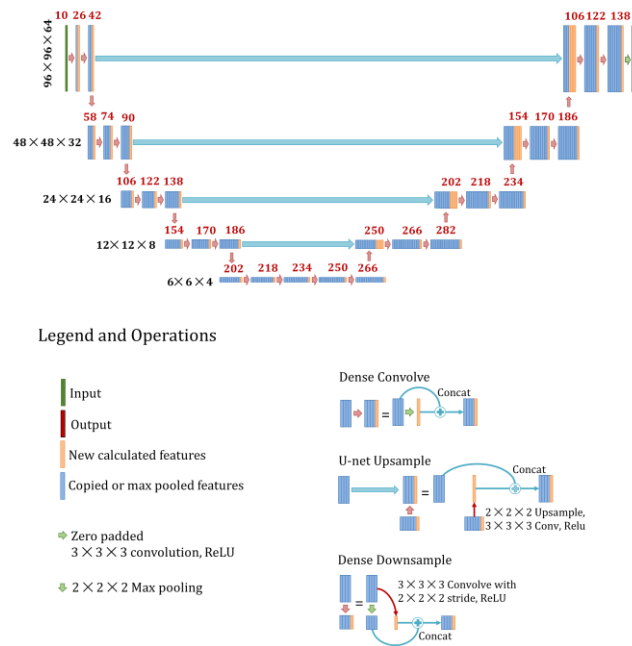


Figure 1. Architecture of the HD U-Net used in this study. Black numbers on the left side of the model represent the volume shape and resolution at a specific hierarchy. Red numbers represent the number of feature maps at a particular layer. Orange features represent the newly calculated features, and trainable parameters to learn, while blue features are copied or max pooled features that do not need trainable parameters. The number of features (red numbers) represented here corresponds to the model including both anatomical and beam setup information (*AB model*, 10 input channels).

2. B. Patient database

The database consisted on 129 lung cancer patients treated with IMRT in UT Southwestern Medical Center, which involved four different treating physicians. The database was heterogeneous in terms of number of beams and orientation (**Figure 2** and **3**), and beam energy (6 and 10 MV). The clinically delivered dose and the contours for each patient was extracted from two different treatment planning systems: Pinnacle V8.0-V9.6 (Philips Radiation Oncology Systems, Fitchburg, WI) for patients treated prior to 2017 and Eclipse V13.7-V15.5 (Varian Medical Systems, Palo Alto, CA) for patients treated after to 2017. All plans were created and calculated with heterogeneity correction. The target dose prescription was 60 Gy for all patients, but two different fractionations protocols were included: 4 Gy x 15 fractions and 2 Gy x 30 fractions. The original IMRT dose and the contours masks for all patients were resampled to have a voxel resolution of 5x5x5 mm³.

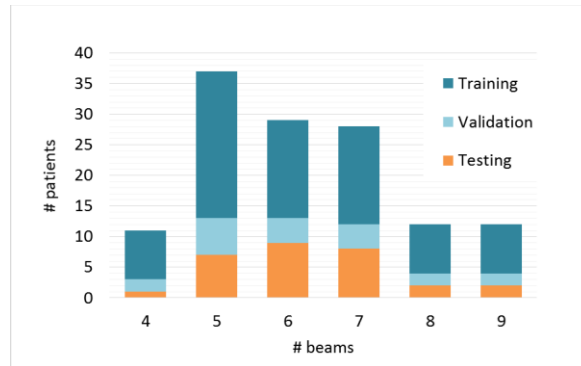


Figure 2. Number of patients per beam configuration (ranging from 4 to 9 beams) used for training (upper bar), validation (middle bar), and testing (lower bar).

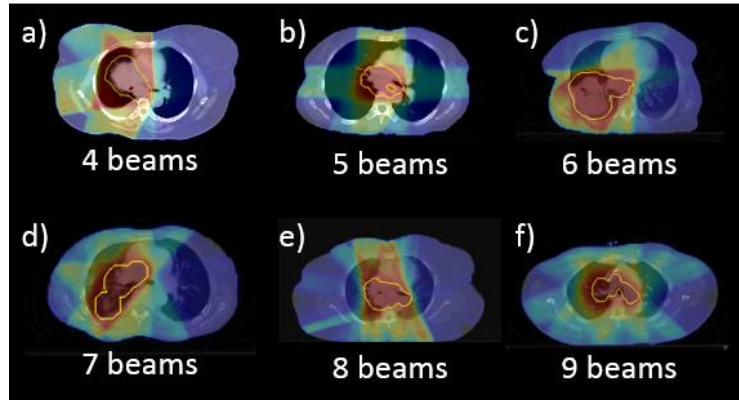


Figure 3. Examples of the different beam configurations from the patient database (test set). The yellow contour represents the PTV volume and the color wash the dose distribution.

2. C. Model performance

In order to evaluate the performance and stability of the model, the database was divided in two sets: 1) 100 patients for training and cross validation (**Figure 2**, upper and middle bars), and 2) 29 patients for testing (**Figure 2**, lower bars). A 5-fold cross validation procedure was applied to the 100 patients set, which was itself split in 80 patients for training and 20 patients for validation (**Figure 2**), alternating the latter along the 5-folds. The partitions

were always done by trying to keep a good balance between the number of patients per beam configuration in the three listed sets: training, validation and testing (**Figure 2**). The number of patients of each beam configuration class was the same for each cross-validation fold. At every iteration, the network weights are updated based on the 80 training patients, and the loss function is computed on the validation set. The final model is selected as the one corresponding to the iteration with lower validation loss, in order to avoid overfitting to the training data⁴⁸. This process is repeated for each fold, generating 5 final models that will then be evaluated in the testing data set. All these operations were performed on an NVIDIA TESLA K80 GPU with 12 GB dedicated RAM.

The *AB model* was also compared with our previous work and current state-of-the-art, the *anatomy only* (AO) model, which contains 9 input channels for the PTV and organs, without the beam setup information. The accuracy of the two methods (*AB* and *AO*) was evaluated by computing the average error between the predicted ($D_{p,AB}$ and $D_{p,AO}$) and clinically delivered (D_c) dose distributions, on the mean and maximum dose values for different organs. The average error on relevant DVH metrics were also analyzed, such as the lung volume receiving a dose of at least 20 Gy (V_{20}) or the dose delivered to 95% of the target volume (D_{95}), among others. All these values are presented as a percentage of the prescribed target dose (60 Gy). For easier comparison among patients, all doses ($D_{p,AB}$, $D_{p,AO}$, and D_c) were normalized to have an average dose inside the PTV equal to the prescription dose, i. e., $D_{mean} = 60\text{Gy}$. This normalization point serves just as a fixed point for comparison, but the user can later shift the dose to any other convenient reference, such as the D_{95} of PTV equal to the prescription dose, which is often used in the clinic. The target dose homogeneity was also evaluated using the following equation for the homogeneity index: $HI = (D_2 - D_{98})/D_{50}$. In addition, Dice similarity coefficients of the isodose volumes from 5% to 95% of the prescription dose were also computed for $D_{p,AB}$ and $D_{p,AO}$ and compared with those for D_c , to evaluate the accuracy of the spatial distribution of the dose predicted by the two models.

2. D. Beam configuration representation

The proposed architecture (section 2.A) aims to improve the accuracy and robustness of the dose prediction against a very heterogeneous database regarding beam arrangement. The key here is how to best represent the beam configuration without greatly complicating the model architecture, and in the meanwhile, providing valuable information for accurate dose distribution prediction. Ideally, a good representation should be in the dose domain, contain information about beam energy, beam aperture, and heterogeneity correction, while being computationally inexpensive. For this purpose, we use a cumulative dose distribution computed using a ray-tracing type of algorithm for all beams in the plan, without modulation, and with apertures conformal to the PTV in beam's eye view. We use a fluence-convolution broad-beam (FCBB) dose calculation method^{49, 50}, which is a modified ray-tracing algorithm, involving a 2D convolution of a fluence map with a lateral spread function followed by ray-tracing based on the central axis of the beam. In our case, a dummy homogeneous fluence map (i.e., all weights equal to 1) with the aperture of the PTV projection in beam's eye view plus an isotropic margin of 5 mm is generated for each beam angle. The FCBB dose engine then uses this dummy fluence map as input, together with percentage depth dose (PDD) profiles from the Golden Beam Data (GBD)⁵¹ provided by Varian Medical Systems, Inc. (Palo Alto, CA)⁵¹, to compute the non-modulated dose per beam. The algorithm is able to generate the dose per beam in fractions of a second. Since the final computed dose per beam is given in arbitrary units, a normalization is performed after summing up all beams, in order to have

the mean dose inside the PTV equal to the prescription dose. After adding up the dose corresponding to every beam, all voxels inside the PTV are overwritten to have a dose equal to the prescription dose.

Note that this study assumes that the number of beams and orientations have been previously determined by the planner, as commonly done in clinical practice, or eventually given by any beam angle optimization algorithm.

3. RESULTS

The results for the average absolute error and its standard deviation (SD) on the mean and maximum dose for the target and OARs are presented in **Figure 4** for cross-validation (average prediction on the validation set for all 5 folds), and **Figure 5** for testing (average prediction on the test set for all 5 folds). In both cases, the *AB model* reduced the error on the mean and maximum dose around 1% on average, with respect to the *AO model*. The mean dose error value for the test set, averaged across all organs, was equal to $2.28 \pm 2.01\%$ in the *AO model*, versus $1.39 \pm 1.27\%$ in the *AB model*. Likewise, the mean error on the maximum dose for the test set, averaged across all organs, decreased from $3.97 \pm 4.73\%$ for the *AO model* to $2.85 \pm 3.06\%$ for the *AB model*. The biggest improvement was found for the spinal cord maximum dose, where the *AB model* reduced the prediction error up to 3.6% for cross-validation and 2.6% for testing, with respect to the *AO model*. **Table 1** reports some relevant DVH metrics commonly used in clinic to evaluate lung IMRT treatments, predicted from the two models. Again, the *AB model* outperforms the *AO model*, with improved prediction accuracy for all considered DVH metrics. Although the difference in the mean average error for most metrics is rather low (around 1 - 1.5%), for some other metrics such as the lungs V_{20} or V_5 , the error decreased up to 2% and 5%, respectively. The spinal cord D_2 was also significantly decreased (around 3%).

The dose distribution in the target volume was predicted with equivalent accuracy by the two models, with homogeneity index (HI, mean \pm SD) equal to 0.11 ± 0.02 for the *AO model* and 0.08 ± 0.02 for the *AB model*, versus 0.09 ± 0.04 for the clinical doses, for cross-validation. Similar results were obtained for testing, i.e., HI equal to 0.10 ± 0.03 for the *AO model* and 0.08 ± 0.02 for the *AB model*, versus 0.09 ± 0.03 for the clinical doses.

Dice similarity coefficients for the isodose volumes in D_c versus $D_{p,AB}$ (blue) and $D_{p,AO}$ (red), respectively, are presented in **Figure 6**. The *AB model* clearly outperforms the *AO model*, with most isodose volumes having a Dice coefficient equal or above 0.9, for both cross-validation and testing. In particular, the *AO model* shows a poor accuracy for the isodose volumes in the medium to low dose region, i.e., Dice < 0.9 for the isodose volumes up to 60-70% of the prescription dose, while the *AB model* achieves a Dice about 10% higher in the same region. In contrast, the high dose region (from 80% isodose line onwards) is predicted with comparable accuracy in both models, although the *AB model* keeps being slightly superior, with Dice coefficients up to 2.5-5% higher. The lowest prediction accuracy occurs around the 40% isodose line for both $D_{p,AB}$ and $D_{p,AO}$, but this effect appears to be much more pronounced in the *AO model*. In addition, the color-wash band representing the standard deviation of the Dice coefficient across all patients is also narrower for the *AB model* for both cross-validation and testing, indicating a more stable model.

Figure 6 also includes the Dice similarity coefficients for the isodose volumes in D_c versus the input channel containing the beam representation for the *AB model*, i.e., the cumulated FCBB dose for all beams with the overwritten values inside the PTV equal to the prescription dose (Section 2.D). The FCBB dose alone seems to be an excellent

approximation of D_c in the low and medium dose region, with a Dice value about 0.9. The difference between the prediction from the *AB model* and its input channel is nearly zero up to the 20% isodose volume and starts to increase after this point (**Figures 6.c** and **6.d.**, yellow curve). This indicates that the *AB model* uses the input channel information as it is, without further modification, and learn how to include the modulation in the dose for each beam from the 20% isodose volume onwards.

As illustration of the three-dimensional dose distribution predicted by the two models, the results for one of the test patient is presented in **Figure 7**, for an axial slice located at the center of the target, as well as the corresponding DVH for D_c , $D_{p,AB}$ and $D_{p,AO}$. The rest of the patients are not presented here due to limited space in the manuscript, but the behavior is similar for all of them: the *AO model* predictions show a very isotropic dose gradient that uniformly decreases from the target till the edge of the body, while the *AB model* is able to capture the dose features along the beam path due to the additional beam setup information.

The two models, *AO* and *AB*, were trained during 150 epochs, which took about 15 hours in both cases. Additional training for a larger number of epochs was investigated but did not result in significant improvement. The average prediction time and its standard deviation was 11.42 ± 0.12 s per patient for the *AO model*, and 11.66 ± 0.14 s for the *AB model*, using one NVIDIA Tesla K80 card. The convergence of the two models is presented in **Figure 8**. The initial mean squared error for training and validation is much lower in the *AB model* (< 5) than in the *AO model* (> 14). This indicates that the prediction from the *AB model* is closer to the ground truth from the beginning, thanks to the extra input channel containing the beam setup information.

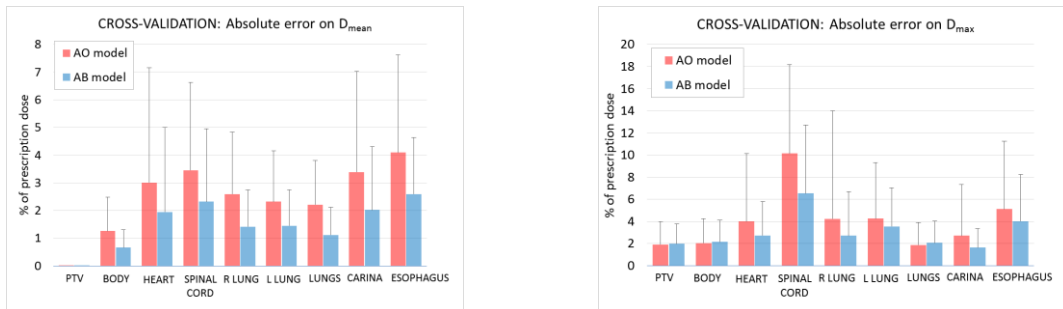


Figure 4. Average absolute error on the mean (left) and maximum dose (right) for the predictions ($D_{p,AB}$ and $D_{p,AO}$) versus the clinical dose (D_c) of all 5-fold models on the corresponding validation set, for relevant organs in lung treatments. The black lines on top of the bars represent the standard deviation associated to each organ.

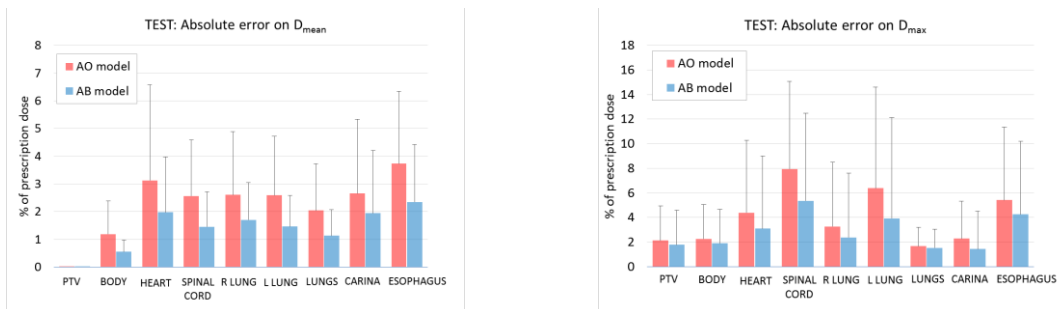


Figure 5. Average absolute error on the mean (left) and maximum dose (right) for the predictions ($D_{p,AB}$ and $D_{p,AO}$) versus the clinical dose (D_c) of all 5-fold models on the test set, for relevant organs in lung treatments. The black lines on top of the bars represent the standard deviation associated to each organ.

Table 1. Mean absolute error and its standard deviation (mean \pm SD) for relevant DVH metrics on the target and several organs, for cross-validation (average prediction on the validation set for all 5 folds), and testing (average prediction on the test set for all 5 folds), for the *AO* and *AB model*. The values are expressed as percentage of the prescription dose ($D_{pre} = 60$ Gy) for the metrics reporting the dose received by x% of volume (D_x), and as absolute difference for the metrics reporting the volume (in %) receiving a dose of y Gy (V_y).

Absolute mean error for DVH metrics					
		Cross-validation (mean \pm SD)		Testing (mean \pm SD)	
		<i>AO model</i>	<i>AB model</i>	<i>AO model</i>	<i>AB model</i>
PTV	D₉₉ (% of D_{pre})	3.36 \pm 3.24	2.70 \pm 3.06	3.50 \pm 2.96	2.54 \pm 2.56
	D₉₈ (% of D_{pre})	2.61 \pm 2.15	1.95 \pm 2.09	2.61 \pm 2.20	1.71 \pm 1.73
	D₉₅ (% of D_{pre})	1.80 \pm 1.25	1.10 \pm 0.86	1.92 \pm 1.34	1.08 \pm 0.96
	D₅ (% of D_{pre})	0.97 \pm 0.83	0.81 \pm 0.75	1.10 \pm 1.50	0.94 \pm 0.74
Esophagus	D₂ (% of D_{pre})	5.39 \pm 7.13	4.10 \pm 4.61	6.04 \pm 6.23	4.74 \pm 4.85
	V₄₀ (% of volume)	4.99 \pm 5.57	3.25 \pm 3.77	4.74 \pm 5.09	3.58 \pm 4.90
	V₅₀ (% of volume)	4.94 \pm 5.45	3.65 \pm 4.31	4.14 \pm 4.09	2.56 \pm 2.94
Heart	V₃₅ (% of volume)	3.40 \pm 7.78	2.48 \pm 6.29	3.32 \pm 5.41	2.57 \pm 4.76
Spinal cord	D₂ (% of D_{pre})	10.10 \pm 7.82	6.74 \pm 6.10	7.64 \pm 7.12	5.05 \pm 4.10
Lungs	D_{mean} (% of D_{pre})	2.21 \pm 1.61	1.12 \pm 1.00	2.04 \pm 1.68	1.13 \pm 0.94
	V₅ (% of volume)	7.48 \pm 6.14	2.60 \pm 3.37	8.20 \pm 7.06	2.67 \pm 2.61
	V₂₀ (% of volume)	3.96 \pm 3.66	2.18 \pm 2.42	4.66 \pm 4.51	2.67 \pm 2.87

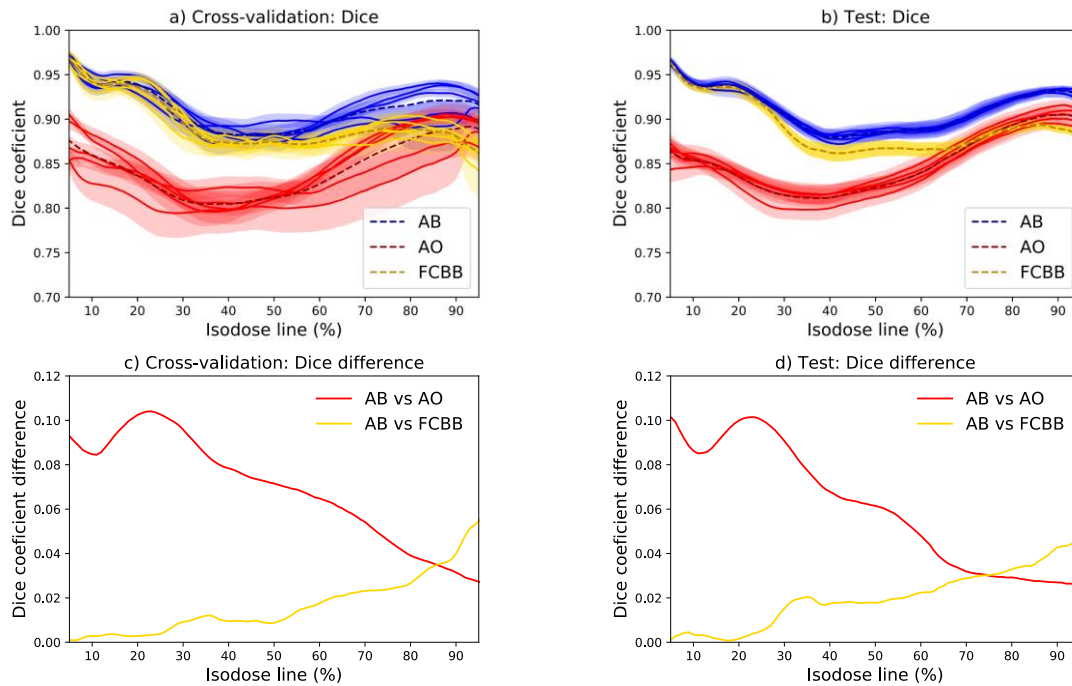


Figure 6. The upper plots (a. and b.) contain the Dice similarity coefficients of the isodose volumes from 5% to 95% of the prescription dose for $D_{p,AB}$ (solid blue lines), $D_{p,AO}$ (solid red lines), and the input channel of the *AB model* containing the FCBB dose (solid yellow lines), versus D_c , together with their corresponding average (dashed line) and standard deviation (color wash), for the 5-fold cross-validation (left) and testing (right). The bottom plots (c. and d.) contain the difference between the averaged Dice coefficient from the *AB model* versus the *AO model* (red line) and the FCBB dose used as input for the *AB model* (yellow line).

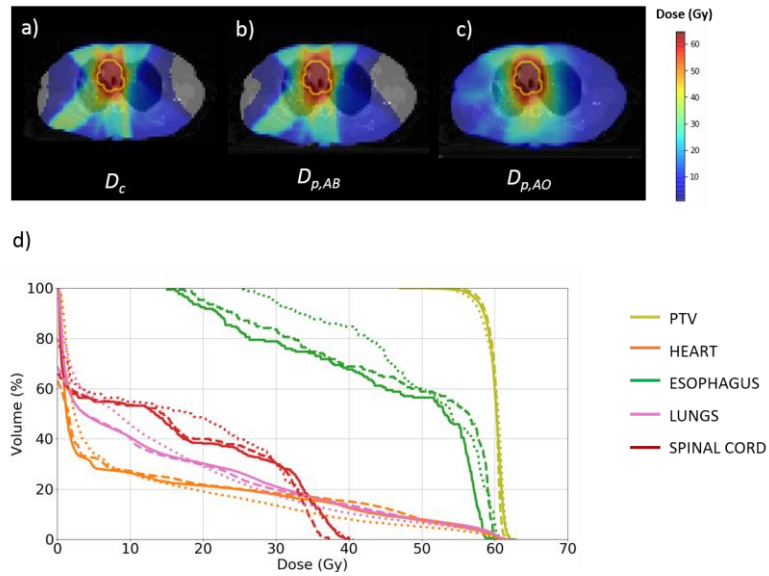


Figure 7. Illustration of an axial slice at the center of the target volume for one of the test patients: **a)** clinical dose (D_c), **b)** predicted dose from the AB model ($D_{p,AB}$), and **c)** predicted dose from the AO model ($D_{p,AO}$). Bottom plot (d) contain the DVHs for the three doses, solid lines correspond to the clinical dose (D_c), dashed lines to the prediction from AB model ($D_{p,AB}$), and dotted lines correspond to the prediction from the AO model ($D_{p,AO}$).

Average Training Loss (solid) and Validation Loss (dotted)

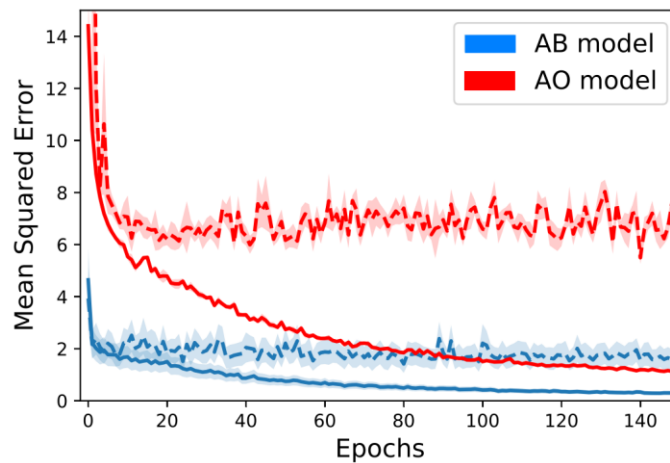


Figure 8. Loss function (mean squared error) evaluated for the training (solid lines) and validation sets (dotted lines), for the AO (red) and AB model (blue). The lines correspond to the average value of the loss function, for all the 5 models obtained after the 5-fold cross-validation process, while the color-wash bands represent the associated standard deviation.

4. DISCUSSION

The *AB model* outperformed the *AO model* in all the considered evaluation criteria, i.e., DVH metrics and Dice similarity coefficients for the isodose surfaces. The improvement in the high dose region was rather small (around 1% of the prescription dose, on average), but major differences were found for the medium to low dose regions (up to the 60-70% isodose lines), where the beam information actually plays an important role. For this region, the *AB model*

presented a Dice coefficient 10% superior than the *AO model*. Another example of the improved prediction accuracy of the *AB model* for the low dose region is the lung volume receiving at least 5 Gy (V_5), for which the prediction error was decreased up to 5% with respect to the *AO model*. The visual inspection of the predicted dose distributions from the two models also confirmed these results. The predictions from the *AO model* were unable to capture the dose features along the beam path, leading to a very uniform and isotropic dose fall-off. In contrast, the *AB model* presented in this work predicted accurately the dose fingers corresponding to the different beam geometries.

The *AB model* was then able to learn from a very heterogeneous database in terms of beam configuration, by incorporating both anatomical and beam geometry information into the network. Our results suggest that by representing the beam configuration in the dose domain we provide the model with valuable information about the dosimetric features that are not consistent through the database, due to the variable beam arrangement. The FCBB dose calculation used in this work is an improved ray-tracing type of algorithm, but we believe that any other elementary dose calculation algorithm can be used for the same purpose. Thus, the *AB model* represents an important step forward towards an easier and more robust implementation of automatic planning techniques, since it reduces the model dependence on consistent beam configuration characteristics through the training patient database. This is especially true for lung IMRT treatments, where tumors occur in different positions in the thorax and its spatial relationship with other critical organs strongly varies from patient to patient, causing more variability in beam setup compared to other tumor sites, such as prostate, where the beam configuration is relatively stable. Many other type of treatments could also benefit from this improved robustness against variable beam configuration, such as IMRT - 4π treatments for brain⁵² or liver^{53,54}, among others⁵⁵⁻⁵⁷.

Regarding previous studies from other groups, the results obtained from the *AB model* (average error for the mean dose equal to 1.39 ± 1.27 %) are consistent with the values reported by McIntosh and Purdie³⁷, who achieved a mean average difference for their lung test set equal to 1.33%, using a homogeneous beam configuration (all patients treated with VMAT). They did not report the prediction error for the maximum dose, which is often more challenging to predict than the mean dose, but we consider that our model achieved an excellent accuracy for this metric too, since the average for all organs was equal to 2.85 ± 3.06 % for the test set. In addition, the prediction of the low dose region may be improved thanks to the supplementary beam setup information, even for models that used the same beam configuration for all patients in the database. For instance, Moore et al.³⁴ reported up to 20 Gy of difference between predicted and real dose, for regions that were far away from the PTV, using a database where all patients (prostate and brain) were treated with VMAT.

The time needed to predict the three-dimensional dose distribution per patient was not significantly higher for the *AB model* (11.66 ± 0.14 s) than for the *AO model* (11.42 ± 0.12 s). The time employed to compute the FCBB dose used as input to the model can be considered negligible since it was less than one second⁵⁰. In addition, the FCBB dose per beam can later be used to feed the optimizer⁴⁹ in the treatment planning system employed to generate the plan. The predicted 3D dose matrix shall then be used as a voxel-wise objective to create a treatment plan that mimics it^{35,41,43}. Since the most advanced optimizers can provide a solution within seconds, the total time required to generate a full plan may be kept under a minute, if the right hardware is used. This provides a good environment to implement online adaptive strategies⁹, where the plan needs to be adapted while the patient is on the treatment couch, and every few extra minutes are of crucial importance. In addition, the presented model could be used as part of beam angle optimization strategies for IMRT, by generating 3D doses for

different beam configurations and then selecting the optimal one according to DVH metrics or any other relevant criteria used in the clinic for plan evaluation. In this context, the generated doses could also serve as a planning guidance for the dosimetrist, or even as decision support tool for the treating physician, before going to treatment planning. Eventually, the dose prediction model could be used in the tumor board meetings for previous comparison with other suitable treatments, and assist in the evaluation of tumor control probability and possible secondary effects.

Lastly, the dose prediction models existing in literature have been applied so far to radiation therapy treatments with photons, i.e., IMRT or VMAT. However, extending these models to proton therapy represents an extra challenge, given the sensibility of the dose distribution to the heterogeneities in the traversed tissue. In this context, providing the model with basic beam setup information along the beam path is a must, and we believe our model could be easily applied for that purpose, which we plan to study in a future work.

5. CONCLUSION

Deep neural networks were used to build a model that is able to learn from a database of previous clinical cases treated with variable beam configuration, and predict the three-dimensional dose distribution for a new patient. Two models were trained and compared, the first model contained input information which only accounted for the anatomy of the patient, while the second model included both anatomical and beam setup information, the latter being represented in the dose domain. The second model showed an improved accuracy and robustness against variable beam geometry, with respect to the first one. This suggests the use of a three-dimensional matrix containing elementary dose features along the beam paths as input to the model, in order to achieve a more comprehensive automatic planning based on deep neural networks, without the need of training specific models for every different beam arrangement.

ACKNOWLEDGEMENTS

Ana Barragán Montero is supported by Fonds Baillet-Latour.

REFERENCES

- ¹ U. Oelfke and T. Bortfeld, Inverse planning for photon and proton beams, *Med. Dosim.* (2001).
- ² V. Baturalai, M.G. Jameson, D.F. Forstner, P. Vial, and L.C. Holloway, How important is dosimetrist experience for intensity modulated radiation therapy? A comparative analysis of a head and neck case, *Pract. Radiat. Oncol.* (2013).
- ³ S.L. Berry, A. Boczkowski, R. Ma, J. Mechalakos, and M. Hunt, Interobserver variability in radiation therapy plan output: Results of a single-institution study, *Pract. Radiat. Oncol.* (2016).
- ⁴ B.E. Nelms, G. Robinson, J. Markham, *et al.*, Variation in external beam treatment plan quality: An inter-institutional study of planners and planning systems, *Pract. Radiat. Oncol.* (2012).
- ⁵ M. Marcello, M. Ebert, A. Haworth, *et al.*, Association between treatment planning and delivery factors and disease progression in prostate cancer radiotherapy: Results from the TROG 03.04 RADAR trial, *Radiother. Oncol.* (2018).
- ⁶ L.J. Peters, B. O'Sullivan, J. Giralt, *et al.*, Critical impact of radiotherapy protocol

compliance and quality in the treatment of advanced head and neck cancer: Results from TROG 02.02, *J. Clin. Oncol.* (2010).

7 K.L. Moore, R. Schmidt, V. Moiseenko, *et al.*, Quantifying unnecessary normal tissue complication risks due to suboptimal planning: A secondary study of RTOG 0126, *Int. J. Radiat. Oncol. Biol. Phys.* (2015).

8 D. Yan, F. Vicini, J. Wong, and A. Martinez, Adaptive radiation therapy, *Phys. Med. Biol.* (1997).

9 S. Lim-Reinders, B.M. Keller, S. Al-Ward, A. Sahgal, and A. Kim, *Online Adaptive Radiation Therapy*, *Int. J. Radiat. Oncol. Biol. Phys.* (2017).

10 J.A. González Ferreira, J. Jaén Olasolo, I. Azinovic, and B. Jeremic, *Effect of radiotherapy delay in overall treatment time on local control and survival in head and neck cancer: Review of the literature*, *Reports Pract. Oncol. Radiother.* (2015).

11 H. Yang, W. Hu, W. Wang, P. Chen, W. Ding, and W. Luo, Replanning during intensity modulated radiation therapy improved quality of life in patients with nasopharyngeal carcinoma, *Int. J. Radiat. Oncol. Biol. Phys.* (2013).

12 C. A.M., Y. T., H. S., and M. A., Image-guided adaptive radiotherapy improves acute toxicity during intensity-modulated radiation therapy for head and neck cancer, *J. Radiat. Oncol.* (2018).

13 D.S. Møller, M.I. Holt, M. Alber, *et al.*, Adaptive radiotherapy for advanced lung cancer ensures target coverage and decreases lung dose, *Radiother. Oncol.* (2016).

14 S. Breedveld, P.R.M. Storchi, P.W.J. Voet, and B.J.M. Heijmen, ICycle: Integrated, multicriterial beam angle, and profile optimization for generation of coplanar and noncoplanar IMRT plans, *Med. Phys.* (2012).

15 I. Xhaferllari, E. Wong, K. Bzdusek, M. Lock, and J.Z. Chen, Automated IMRT planning with regional optimization using planning scripts, *J. Appl. Clin. Med. Phys.* (2013).

16 T.G. Purdie, R.E. Dinniwell, A. Fyles, and M.B. Sharpe, Automation and intensity modulated radiation therapy for individualized high-quality tangent breast treatment plans, *Int. J. Radiat. Oncol. Biol. Phys.* (2014).

17 X. Zhang, X. Li, E.M. Quan, X. Pan, and Y. Li, A methodology for automatic intensity-modulated radiation treatment planning for lung cancer, *Phys. Med. Biol.* (2011).

18 D.L. Craft, T.S. Hong, H.A. Shih, and T.R. Bortfeld, Improved planning time and plan quality through multicriteria optimization for intensity-modulated radiotherapy, *Int. J. Radiat. Oncol. Biol. Phys.* (2012).

19 S. Breedveld, D. Craft, R. van Haveren, and B. Heijmen, *Multi-criteria optimization and decision-making in radiotherapy*, *Eur. J. Oper. Res.* (2018).

20 B. Wu, F. Ricchetti, G. Sanguineti, *et al.*, Data-driven approach to generating achievable dose-volume histogram objectives in intensity-modulated radiotherapy planning, *Int. J. Radiat. Oncol. Biol. Phys.* (2011).

21 L.M. Appenzoller, J.M. Michalski, W.L. Thorstad, S. Mutic, and K.L. Moore, Predicting dose-volume histograms for organs-at-risk in IMRT planning, *Med. Phys.* (2012).

22 L. Yuan, Y. Ge, W.R. Lee, F.F. Yin, J.P. Kirkpatrick, and Q.J. Wu, Quantitative analysis of the factors which affect the interpatient organ-At-risk dose sparing variation in IMRT plans, *Med. Phys.* (2012).

23 X. Zhu, T. li, D. Thongphiew, Y. ge, F. Yin, and Q. wu, TU-E-BRB-03: A Planning Quality Evaluation Tool for Adaptive IMRT Treatment Based on Machine Learning, in *Med. Phys.*(2010).

24 J. Krayenbuehl, I. Norton, G. Studer, and M. Guckenberger, Evaluation of an automated knowledge based treatment planning system for head and neck, *Radiat. Oncol.* (2015).

25 A.T.Y. Chang, A.W.M. Hung, F.W.K. Cheung, *et al.*, Comparison of Planning Quality and Efficiency Between Conventional and Knowledge-based Algorithms in Nasopharyngeal Cancer Patients Using Intensity Modulated Radiation Therapy, in *Int. J. Radiat. Oncol. Biol. Phys.*(2016).

26 B. Vanderstraeten, B. Goddeeris, K. Vandecasteele, M. van Eijkeren, C. De Wagter,

- and Y. Lievens, Automated Instead of Manual Treatment Planning? A Plan Comparison Based on Dose-Volume Statistics and Clinical Preference, *Int. J. Radiat. Oncol. Biol. Phys.* (2018).
- 27 C.R. Hansen, A. Bertelsen, I. Hazell, *et al.*, Automatic treatment planning improves the clinical quality of head and neck cancer treatment plans, *Clin. Transl. Radiat. Oncol.* (2016).
- 28 M. Hussein, C.P. South, M.A. Barry, *et al.*, Clinical validation and benchmarking of knowledge-based IMRT and VMAT treatment planning in pelvic anatomy, *Radiother. Oncol.* (2016).
- 29 P.W.J. Voet, M.L.P. Dirkx, S. Breedveld, A. Al-Mamgani, L. Incrocci, and B.J.M. Heijmen, Fully automated volumetric modulated arc therapy plan generation for prostate cancer patients, *Int. J. Radiat. Oncol. Biol. Phys.* (2014).
- 30 J.P. Tol, A.R. Delaney, M. Dahele, B.J. Slotman, and W.F.A.R. Verbakel, Evaluation of a knowledge-based planning solution for head and neck cancer, *Int. J. Radiat. Oncol. Biol. Phys.* (2015).
- 31 A.R. Delaney, J.P. Tol, M. Dahele, J. Cuijpers, B.J. Slotman, and W.F.A.R. Verbakel, Effect of Dosimetric Outliers on the Performance of a Commercial Knowledge-Based Planning Solution, *Int. J. Radiat. Oncol. Biol. Phys.* (2016).
- 32 B. Wu, M. Kusters, M. Kunze-busch, *et al.*, Cross-institutional knowledge-based planning (KBP) implementation and its performance comparison to Auto-Planning Engine (APE), *Radiother. Oncol.* (2017).
- 33 L. Yuan, W. Zhu, Y. Ge, *et al.*, Lung IMRT planning with automatic determination of beam angle configurations, *Phys. Med. Biol.* (2018).
- 34 S. Shiraishi and K.L. Moore, Knowledge-based prediction of three-dimensional dose distributions for external beam radiotherapy, *Med. Phys.* (2016).
- 35 C. McIntosh, M. Welch, A. McNiven, D.A. Jaffray, and T.G. Purdie, Fully automated treatment planning for head and neck radiotherapy using a voxel-based dose prediction and dose mimicking method, *Phys. Med. Biol.* (2017).
- 36 C. McIntosh and T.G. Purdie, Contextual Atlas Regression Forests: Multiple-Atlas-Based Automated Dose Prediction in Radiation Therapy, *IEEE Trans. Med. Imaging* (2016).
- 37 C. McIntosh and T.G. Purdie, Voxel-based dose prediction with multi-patient atlas selection for automated radiotherapy treatment planning, *Phys. Med. Biol.* (2017).
- 38 D. Nguyen, X. Jia, D. Sher, *et al.*, Three-Dimensional Radiotherapy Dose Prediction on Head and Neck Cancer Patients with a Hierarchically Densely Connected U-net Deep Learning Architecture, (2018).
- 39 D. Nguyen, T. Long, X. Jia, *et al.*, Dose Prediction with U-net: A Feasibility Study for Predicting Dose Distributions from Contours using Deep Learning on Prostate IMRT Patients, (2017).
- 40 X. Chen, K. Men, Y. Li, J. Yi, and J. Dai, A feasibility study on an automated method to generate patient-specific dose distributions for radiotherapy using deep learning, *Med. Phys.* (2018).
- 41 J. Fan, J. Wang, Z. Chen, C. Hu, Z. Zhang, and W. Hu, Automatic treatment planning based on three-dimensional dose distribution predicted from deep learning technique, *Med. Phys.* (2018).
- 42 V. Kearney, J.W. Chan, S. Haaf, M. Descovich, and T.D. Solberg, DoseNet: a volumetric dose prediction algorithm using 3D fully-convolutional neural networks, *Phys. Med. Biol.* **63**, (2018).
- 43 T. Long, M. Chen, S. Jiang, and W. Lu, Threshold-driven optimization for reference-based auto-planning, *Phys. Med. Biol.* (2018).
- 44 O. Ronneberger, P. Fischer, and T. Brox, U-net: Convolutional networks for biomedical image segmentation, in *Lect. Notes Comput. Sci. (including Subser. Lect. Notes Artif. Intell. Lect. Notes Bioinformatics)* (2015).
- 45 E. Shelhamer, J. Long, and T. Darrell, Fully Convolutional Networks for Semantic Segmentation, *IEEE Trans. Pattern Anal. Mach. Intell.* (2017).

- 46 G. Huang, Z. Liu, L. Van Der Maaten, and K.Q. Weinberger, Densely connected
convolutional networks, in *Proc. - 30th IEEE Conf. Comput. Vis. Pattern Recognition,*
47 *CVPR 2017*(2017).
- 48 F. Milletari, N. Navab, and S.A. Ahmadi, V-Net: Fully convolutional neural networks for
volumetric medical image segmentation, in *Proc. - 2016 4th Int. Conf. 3D Vision, 3DV*
2016(2016).
- 49 R. Caruana, S. Lawrence, and L. Giles, Overfitting in neural nets: Backpropagation,
conjugate gradient, and early stopping, *Nips-2000* (2000).
- 50 W. Lu, A non-voxel-based broad-beam (NVBB) framework for IMRT treatment
planning, *Phys. Med. Biol.* (2010).
- 51 W. Lu and M. Chen, Fluence-convolution broad-beam (FCBB) dose calculation, *Phys.*
Med. Biol. (2010).
- 52 G.P. Beyera, Commissioning measurements for photon beam data on three
TrueBeam linear accelerators, and comparison with Trilogy and Clinac 2100 linear
accelerators, *J. Appl. Clin. Med. Phys.* (2013).
- 53 V.L. Murzin, K. Woods, V. Moiseenko, *et al.*, 4 π plan optimization for cortical-sparing
brain radiotherapy, *Radiother. Oncol.* (2018).
- 54 D. P., L. T., R. D., *et al.*, 4PI radiation therapy for liver SBRT, *Int. J. Radiat. Oncol.*
Biol. Phys. (2012).
- 55 K. Woods, D. Nguyen, A. Tran, *et al.*, Viability of Noncoplanar VMAT for liver SBRT
compared with coplanar VMAT and beam orientation optimized 4 π IMRT, *Adv.*
Radiat. Oncol. (2016).
- 56 J.C.M. Rwigema, D. Nguyen, D.E. Heron, *et al.*, 4 π noncoplanar stereotactic body
radiation therapy for head-and-neck cancer: Potential to improve tumor control and
late toxicity, *Int. J. Radiat. Oncol. Biol. Phys.* (2015).
- 57 D. Nguyen, J.C.M. Rwigema, V.Y. Yu, *et al.*, Feasibility of extreme dose escalation for
glioblastoma multiforme using 4 π radiotherapy, *Radiat. Oncol.* (2014).
- A. Tran, J. Zhang, K. Woods, *et al.*, Treatment planning comparison of IMPT, VMAT
and 4 π radiotherapy for prostate cases, *Radiat. Oncol.* (2017).